Prediction of airborne sound transmission across a timber-concrete composite floor using Statistical Energy Analysis

Claire Churchill and Carl Hopkins

Prediction of airborne sound transmission across a timber-concrete composite floor using Statistical Energy Analysis

Prediction of airborne sound transmission across a timber-concrete composite floor using Statistical Energy Analysis

Claire Churchill[1] and Carl Hopkins[2]*

[1] EMPA, Laboratory for Acoustics/Noise Control, Überlandstrasse 129, 8600 Dübendorf, Switzerland

[2] Acoustics Research Unit, School of Architecture, University of Liverpool, Liverpool L69 7ZN, UK

*Corresponding author

Email: carl.hopkins@liverpool.ac.uk

Abstract

This paper concerns the development and experimental validation of prediction models using Statistical Energy Analysis (SEA) to calculate the airborne sound insulation of a timber-concrete composite floor. The complexity in modelling this floor is due to it having (1) a multilayer upper plate formed from concrete and Oriented Strand Board (OSB), (2) multiple types of rigid connector between the upper plate and the timber joists and (3) a resiliently suspended ceiling. A six-subsystem model treats the concrete-OSB plate as a single subsystem and three different five-subsystem models treat the combination of concrete, OSB and timber joists as a single orthotropic plate subsystem. For the orthotropic plate it is suggested that bending stiffnesses predicted using the theories of Huffington and Troitsky provide a more suitable and flexible approach than that of Kimura and Inoue. All SEA models are able to predict the weighted sound reduction index to within 2dB of the measurement. The average difference (magnitude) between measurements and predictions in one-third octave bands is up to 4dB. These results confirm that SEA can be used to model direct transmission across relatively complex floor constructions. However, this requires the inclusion of measured data in the SEA model, namely the dynamic stiffness of the resilient isolators and the cavity reverberation time.

Keywords: airborne sound insulation; statistical energy analysis; timber; concrete; composite floor

1. Introduction

Timber-frame buildings have potential advantages over traditional masonry and concrete buildings in terms of reduced construction times and higher quality due to pre-fabricated, factory-engineered products. However, traditional timber-frame buildings are not always sufficient for the occupants [1] as they can have inadequate low-frequency airborne and impact sound insulation [2,3], excessive deflection, and excessive vibration [4]. There is the potential to overcome these issues through the use of timber-concrete composite floors which are essentially a hybrid type of lightweight and heavyweight construction [5]. This paper concerns the development and validation of a prediction model for airborne sound insulation across such a timber-concrete composite floor.

When assessing building performance at the design stage it is important to have validated models to predict the sound insulation for direct and flanking transmission. A recent review of the acoustical state-of-the-art for timber buildings concluded that there is no general model available for the prediction of airborne sound insulation for direct transmission across individual walls and floors that has acceptable accuracy [6]. This is primarily because many structures are multilayer structures which incorporate resilient isolators and have relatively complex junctions between the walls and/or floors. However, a model by Guigou-Carter *et al* [7] has been developed to incorporate laboratory measurements on timber-frame walls and floors to calculate the sound insulation *in situ* due to both direct and flanking transmission.

Prediction models based on Statistical Energy Analysis (SEA) models have previously been used to predict airborne sound insulation for timber joist floors [8] or timber stud walls [9,10] where the components were rigidly connected with screws/nails. These showed close agreement with measurements. When the direct and flanking walls are formed from stud walls, SEA has also been used to extend the prediction capability from direct transmission to flanking transmission [11,12]. However, these were basic timber-frame walls or floors without floating floors, resilient isolators and suspended ceilings. Basic timber joist floors are usually used as an internal floor within dwellings; hence they typically have low airborne sound insulation (<40dB R_w). In contrast, the timber-concrete composite floor considered in this paper has significantly higher sound insulation (58dB R_w) and with the addition of a floating floor to provide impact sound insulation it could be used as a separating floor between dwellings.

This paper develops and experimentally validates different prediction models based on SEA for the direct airborne sound insulation across a timber-concrete composite floor. Compared to modelling a basic timber joist floor, the timber-concrete composite floor has the added complexity of having (1) a multilayer upper plate formed from concrete and Oriented Strand Board (OSB), (2) multiple types of rigid connector between the upper plate and the timber joists and (3) a resiliently suspended ceiling. Whilst it is relatively straightforward to identify beam and plate subsystems for an SEA model of a basic timber joist floor, the timber-concrete composite floor is sufficiently complex that it is necessary to consider different approaches to describe the dynamic behaviour of the structural elements.

2. Timber-concrete composite floor construction

A timber-concrete composite floor is built into a sound transmission laboratory in order to measure the airborne sound insulation. This defines the construction to be considered for the SEA modelling in this paper.

A cross-section through the floor construction is shown in Figure 1. The dimensions of the full floor are 5670mm x 4590mm. The base floor is formed from two factory-built composite slabs which consist of 70mm concrete cast on top of 12mm OSB. Each slab is supported by solid timber joists (5670mm long, 260mm deep, 80mm wide) with a joist spacing of 440mm. For structural reasons, the two slabs are rigidly connected using two welded steel plates (120mm x 60mm) with a gap of ≈20mm between the slabs. Circular foam tubes (40mm diameter) are compressed into this gap and a cement skim is applied on top. Before the concrete is cast, nails are used to connect the OSB to the timber joists at 100mm centres. There are additional "shear" connecting strips (≈180mm long, 90mm wide) formed from 2mm thick perforated metal connecting the concrete slab to the timber joists (seven strips per joist). These strips are aligned along the centre line of the joist as shown in Figure 2 and penetrate the concrete by ≈40mm and the joists by ≈40mm. Figure 3 shows that the concrete slab is in contact with one-third of the top of the joist.

The suspended ceiling consisted of 12.5mm plasterboard which is screwed to 24mm thick, 48mm wide, timber noggins at 200mm centres. These noggins are spaced at a distance of 500mm to 550mm (except at the edges where a smaller spacing is needed to support the plasterboard). The noggins are connected to the joists using resilient hangers (Ampack Ampaphon) as shown in Figure 4. The hanger comprised two metal brackets isolated from each other by 6.5mm of rubber where the rubber is in compression under static load. The majority of hangers are fixed at 440mm centres (except where the two slabs are connected where this increased to ≈520mm). This resulted in a total of 56 hangers. In the cavities above the plasterboard, 120mm rock wool ($38kg/m^3$) is installed between the joists just above the plasterboard by cutting it to a size such that it is held in place by friction.

2.1 Laboratory measurement of airborne sound insulation

The test floor is built into a laboratory in order to measure the airborne sound insulation. The two test rooms either side of the floor have volumes of $64m^3$ and $69m^3$. The sound reduction index is measured in both directions according to ISO 10140-2 [13] and the direction-average value is used for comparison with the SEA models.

The laboratory walls are lined in order to suppress flanking transmission. The flanking limit of the laboratory is assessed in terms of the sound reduction index, R, in one-third octave bands between 50Hz and 5kHz using the maximum achievable sound reduction index, R'_{max}. The results show that $(R+15dB) \leq R'_{max}$ although at 4kHz, $(R+10dB) \leq R'_{max}$ and at 5kHz, $(R+7dB) \leq R'_{max}$. Hence between 50Hz and 3.15kHz it can be assumed that flanking transmission is negligible.

3. SEA prediction model

Due to the complexity of the composite floor construction, different SEA models are developed to model the floor construction for comparison with the measurements.

Model 1: The six-subsystem SEA model shown in Figure 5a is formed by considering the concrete-OSB plate as a single subsystem (described in section 6.2) for which the SEA matrix is given by

$$
\begin{bmatrix}
\eta_1 & -\eta_{21} & -\eta_{31} & 0 & 0 & 0 \\
-\eta_{12} & \eta_2 & -\eta_{32} & 0 & 0 & -\eta_{62} \\
-\eta_{13} & -\eta_{23} & \eta_3 & -\eta_{43} & -\eta_{53} & 0 \\
0 & 0 & -\eta_{34} & \eta_4 & -\eta_{54} & -\eta_{64} \\
0 & 0 & -\eta_{35} & -\eta_{45} & \eta_5 & 0 \\
0 & -\eta_{26} & 0 & -\eta_{46} & 0 & \eta_6
\end{bmatrix}
\begin{bmatrix}
E_1 \\ E_2 \\ E_3 \\ E_4 \\ E_5 \\ E_6
\end{bmatrix}
=
\begin{bmatrix}
\dfrac{W_{\text{in}(1)}}{\omega} \\ 0 \\ 0 \\ 0 \\ 0 \\ 0
\end{bmatrix}
\tag{1}
$$

where $W_{\text{in}(1)}$ is the power input into subsystem 1, ω is the angular frequency (rad/s), E_i is the energy of subsystem i, η_{ij} is the Coupling Loss Factor (CLF) from subsystem i to j, and η_i is the Total Loss Factor (TLF) for subsystem i.

Model 2: The five-subsystem SEA model shown in Figure 5b is formed by considering the concrete-OSB plate and the timber joists as a single subsystem with equivalent plate properties. This is considered due to the large number of nails and shear connectors that connect the concrete, OSB and timber joists together. The five-subsystem model requires solution of the following matrix

$$
\begin{bmatrix}
\eta_1 & -\eta_{21} & -\eta_{31} & 0 & 0 \\
-\eta_{12} & \eta_2 & \eta_{32} & -\eta_{42} & 0 \\
-\eta_{13} & -\eta_{23} & \eta_3 & -\eta_{43} & -\eta_{53} \\
0 & -\eta_{24} & \eta_{34} & \eta_4 & -\eta_{54} \\
0 & 0 & -\eta_{35} & -\eta_{45} & \eta_5
\end{bmatrix}
\begin{bmatrix}
E_1 \\ E_2 \\ E_3 \\ E_4 \\ E_5
\end{bmatrix}
=
\begin{bmatrix}
\dfrac{W_{\text{in}(1)}}{\omega} \\ 0 \\ 0 \\ 0 \\ 0
\end{bmatrix}
\tag{2}
$$

Model 2a treats the concrete-OSB plate and the timber joists as an isotropic plate with equivalent thickness, density and Young's modulus as described in section 6.3 following the approach of Kimura and Inoue [14].

Model 2b treats the concrete-OSB plate and the timber joists as an isotropic plate with an effective bending stiffness for the orthotropic plate as described in section 6.4 using the approach of Huffington [15] and Troitsky [16].

Model 2c treats the concrete-OSB plate and the timber joists as an orthotropic plate using the approach of Huffington [15] and Troitsky [16]. This model only applies below the higher of the two

critical frequencies (in directions perpendicular and parallel to the joists) and is described in section 6.4.

The SEA matrix is solved by inverting the loss factor matrix to give the energies in each subsystem. SEA path analysis is also used to compare the relative strengths of transmission paths from the source room (subsystem 1) to the receiving room (subsystem 5) in terms of an energy level difference given by

$$\frac{E_1}{E_5} = \frac{\eta_x \eta_y \dots \eta_5}{\eta_{1x} \eta_{xy} \dots \eta_{z5}}$$

(3)

where x, y and z indicate intermediate subsystems in the transmission path.

Both the matrix solution and path analysis give the energies in the source room (subsystem 1) and receiving room (subsystem 5) which is converted into the sound reduction index, R, using

$$R = 10\lg\left(\frac{E_1}{E_5}\right) + 10\lg\left(\frac{V_1}{V_5}\right) + 10\lg\left(\frac{S}{A}\right)$$

(4)

where V is the room volume, S is the surface area of the floor and A is the absorption area in the receiving room.

4. Calculation of coupling loss factors

4.1 Radiation coupling

For all SEA models, the coupling loss factor that accounts for sound radiation from a plate (e.g. subsystems 2 and 4) to a space (e.g. subsystems 1, 3 and 5) is calculated using

$$\eta_{ij} = \frac{\rho_0 c_0 \sigma}{\omega \rho_s}$$

(5)

where ρ_0 is the density of air, c_0 is the speed of sound in air, ρ_s is the mass per unit area of the plate and σ is the frequency-average radiation efficiency (i.e. for high modal density plates) from Leppington et al [17].

The coupling in the reverse direction is calculated using the consistency relationship [8]

$$\frac{\eta_{ij}}{n_j} = \frac{\eta_{ji}}{n_i}$$

(6)

where n is the statistical modal density [8].

For SEA models 1, 2a, and 2b, the frequency-average radiation efficiency from Leppington et al is calculated using $\mu = (f_c / f)^{0.5}$ as follows:

$$\sigma = \frac{U}{2\pi \mu k S \sqrt{\mu^2-1}}\left[\ln\left(\frac{\mu+1}{\mu-1}\right) + \frac{2\mu}{\mu^2-1}\right]\left[C_{BC}C_{OB} - \mu^{-8}(C_{BC}C_{OB} - 1)\right] \quad \text{for } f < f_c$$

(7)

$$\sigma = \frac{1}{\sqrt{1-\mu^2}} \qquad \text{for } f > f_c \tag{8}$$

$$\sigma \approx \left(0.5 - \frac{0.15 L_1}{L_2}\right)\sqrt{k}\sqrt{L_1} \qquad \text{for } f = f_c \tag{9}$$

where U is the plate perimeter, S is the plate area, C_{BC} is a constant for the plate boundary conditions ($C_{BC}=1$ for simply supported boundaries, $C_{BC}=2$ for clamped boundaries), C_{OB} is a constant for the orientation of the baffle that surrounds the edges of the plate ($C_{OB}=1$ when the plate lies within the plane of an infinite rigid baffle, $C_{OB}=2$ when the rigid baffles along the plate perimeter are perpendicular to the plate surface), L_1 is the smaller and L_2 is the larger of the rectangular plate dimensions, L_x and L_y (for square plates, $L_1=L_2=L_x=L_y$).

The radiation efficiency for the frequency band that contains the critical frequency in Eq. (9) can be calculated using $k=2\pi f_c/c_0$.

For SEA model 2c, an estimate for the frequency-average radiation efficiency is needed for one-third octave bands between the two critical frequencies of the orthotropic plate and is calculated using [18]

$$\sigma = \frac{1}{\pi^2}\sqrt{\frac{f_{c1}}{f_{c2}}}\left(\ln\frac{4f}{f_{c1}}\right)^2 \tag{10}$$

where f_{c1} and f_{c2} are the two critical frequencies of the orthotropic plate for which $f_{c1} < f_{c2}$. At f_{c1} there is no validated approach in the literature to calculate the radiation efficiency, therefore measured data using the methodology outlined in [7] with mechanical excitation is used to obtain data for this one-third octave band.

Calculation of the radiation efficiency from Leppington *et al* requires knowledge of the plate boundary conditions (simply supported or clamped) and the orientation of the baffles that affect sound radiation around the edges of the plate. For sound radiation from the concrete-OSB and plasterboard, the calculations assume that the plate boundaries are simply supported and that the walls of the laboratory represent perpendicular baffles. The concrete-OSB plate is installed such that one end of the timber joist rests directly on an individual angle iron whereas the other end rests on rubber isolating mounts on a continuous angle iron connected to the flanking laboratory. The empirical approach for masonry/concrete described by Hopkins [8] (Method No.3) is used in which all calculated values of the radiation efficiency greater than one are set to a value of one.

Separate sheets of plasterboard are joined together with gypsum skim and tape so the plasterboard can be assumed to act as one large plate. For plasterboard, the radiation efficiency near the critical frequency tends to be overestimated; hence all calculated values of the radiation efficiency greater than one are set to a value of one [8].

4.2 Non-resonant coupling between the cavities and the rooms

In order to calculate non-resonant transmission from the cavity to a room across a plate it is necessary to identify the frequency ranges over which the cavity sound field can be described as one-, two- or three-dimensional [8]. The lowest cavity mode is an axial mode which occurs in the 31.5Hz one-third octave band. The first tangential mode occurs across the cavity width (360mm) because the width is larger than the depth, and occurs in the 500Hz one-third octave band. The first cross-cavity mode is the tangential mode across the cavity depth (260mm) which occurs in the 630Hz one-third octave band (this occurs regardless of whether the depth occupied by the noggins and hangers is included in the definition of the cavity depth or not). The first oblique mode occurs in the 800Hz one-third octave band.

For a one- or two-dimensional sound field in the cavity, the coupling loss factor for non-resonant transmission from a cavity (subsystem i) to a room (subsystem j) is given by [19]

$$\eta_{ij} = \frac{\rho_0^2 c_0^3 S \sigma_{f_c}}{\omega^3 V_i \rho_s^2} \tag{11}$$

where S is the surface area of the plate that faces into the cavity, V_i is the volume of subsystem i, and σ_{fc} is the radiation efficiency of the plate assuming the wavespeed in the plate is always equal to that in air which is calculated using Leppington *et al* [17]. An empirical correction is applied in which all calculated values of the radiation efficiency greater than one are set to a value of one [8].

For a three-dimensional sound field in the cavity, the coupling loss factor for non-resonant transmission from a cavity (subsystem i) to a room (subsystem j) is given by [20]

$$\eta_{ij} = \frac{c_0 S}{4 \omega V_i} \tau_{NR} \tag{12}$$

where τ_{NR} is the non-resonant transmission coefficient for the plate that is calculated according to Leppington *et al* [21] and is only defined below the critical frequency of the plate.

The coupling loss factor for non-resonant transmission from the room to the cavity is calculated from the consistency relationship in Eq. (6). In order to assess the transition from Eq. (11) to Eq. (12), both have been used to estimate the coupling loss factor in the 500Hz one-third octave band. The transition from a one- to two- or three-dimensional sound field in the cavity means that there is a discontinuity

in the predictions at 500Hz. Taking the average of the two different models from the SEA matrix solution at 500Hz is used as a pragmatic solution to this problem.

For SEA model 2c which uses an orthotropic plate model, the non-resonant coupling loss factor between the two critical frequencies is also required. For this particular floor, Eq. (11) is used because both critical frequencies are below the first cross-cavity mode of the floor.

The other potential forms of non-resonant coupling correspond to mass-spring-mass resonances. The mass-spring-mass resonance of the system formed by the concrete-OSB (acting as a mass), cavity (acting as an air spring) and the plasterboard (acting as a mass) occurs below 50Hz and therefore it is not included in the SEA model as it is below the frequency range of interest. The mass-spring-mass resonance of the concrete-OSB and joists, resilient hangars and plasterboard is inside the 50Hz one-third octave band; however this band is still included in the SEA model.

4.3 Mechanical coupling across point connections

For point connections between plates and/or beams, the coupling loss factor is given by [22]

$$\eta_{ij} = \frac{N}{\omega m_i} \frac{Re\{Y_j\}}{|Y_i + Y_j + Y_c|^2} \tag{13}$$

where Y_i and Y_j are the driving-point mobilities of subsystems i and j, and Y_c is the mobility of the connector.

Note that Eq. (13) requires the mass of the source subsystem (i.e. a combination of concrete, OSB, and timber joists). For SEA model 2a, an equivalent density and thickness is used to give m_i=3280kg and for SEA models 2b and 2c, the thickness and density of the concrete is used to give m_i=5528kg.

Infinite plate mobilities are commonly used in SEA to give a frequency-independent value for plates where the actual boundary conditions are not known with sufficient accuracy to use an analytical model. The driving-point mobility, Y_{dp}, of a plate for use in Eq. (13) is calculated using

$$Y_{dp} = \frac{1}{8\sqrt{B\rho h}} \tag{14}$$

where B is the bending stiffness, ρ is the plate density and h is the plate thickness.

4.3.1 Rigid point connections

For the concrete-OSB plate, there are nails connecting the OSB to the joists at 100mm centres. To determine the coupling loss factors η_{26} and η_{62} for SEA model 1 these are considered as rigid point connections for which Y_c=0 in Eq. (13).

4.3.2 Resilient hangers

The plasterboard ceiling is suspended by resilient hangers. Assuming each hanger can be represented as a spring with dynamic stiffness, k, the mobility of the connector for use in Eq. (13) is

$$Y_c = \frac{i\omega}{k} \tag{15}$$

The dynamic stiffness of the resilient hangers is measured in the laboratory. For resilient devices used in suspended ceilings, Brunskog and Hammer [23] developed a test rig to quantify the input stiffness and transfer stiffness of devices ranging from hangers to resilient channel systems that are under static load. This measurement system is adopted for the measurements and is shown in Figure 6. It is essentially a mass-spring-mass system where the upper mass is resiliently supported on a separate frame and the lower mass provides a representative static load. The upper mass includes the masses of the wooden noggins. This arrangement accounts for the noggins themselves; hence they are not included as separate subsystems in the SEA model. The upper mass, m_1, weighs 2.56kg and the lower mass, m_2, weighs 10.84kg. This lower mass represents the typical static load applied by one to two layers of plasterboard when suspended by four hangers to ensure that the result is representative of in situ. Excitation is applied to the upper mass using an electrodynamic shaker (Ling Type 201). Broadband noise is used because resonance measurements on resilient elements are prone to non-linear response when using a force hammer [24]. The input force is measured using a force Transducer (PCB Type 208 A04) and the response is measured using accelerometers (PCB Type M352C65) on the underside of the lower and upper masses.

As with measurements of dynamic stiffness using mass-spring-mass systems for wall ties [24], two Frequency Response Functions (FRF) are measured. For these experiments these are the direct and transfer accelerance. Using equivalent circuit theory for lump mass and spring elements for a mass-spring-mass system gives the direct accelerance as [8]

$$\frac{a_1}{F_1} = \frac{k + i\omega R - \omega^2 m_2}{\left[i\omega m_1\left(i\omega m_2 + \frac{k}{i\omega} + R\right)\right] + \left[i\omega m_2\left(\frac{k}{i\omega} + R\right)\right]} \tag{16}$$

and the transfer accelerance as [8]

$$\frac{a_2}{F_1} = \frac{k + i\omega R}{\left[i\omega m_2\left(i\omega m_2 + \frac{k}{i\omega} + R\right)\right] + \left[i\omega m_2\left(\frac{k}{i\omega} + R\right)\right]} \tag{17}$$

where a is the acceleration, F is the force, k is the dynamic stiffness of the resilient device, R is the damping constant of the resilient device, and m is the mass. The subscripts 1 and 2 refer to the upper and lower masses respectively.

For the mass-spring-mass resonance, the damping constant, R, is related to the loss factor, η, by

$$R = \eta \sqrt{k \frac{m_1 m_2}{m_1 + m_2}} \tag{18}$$

Both the direct and transfer accelerance can be used to identify the mass-spring-mass resonance frequency which occurs at

$$f_{\text{resonance}} = \frac{1}{2\pi} \sqrt{\frac{k}{\left(\frac{m_1 m_2}{m_1 + m_2}\right)}} \tag{19}$$

with an anti-resonance that is present in the direct accelerance at

$$f_{\text{anti-resonance}} = \frac{1}{2\pi} \sqrt{\frac{k}{m_2}} \tag{20}$$

Estimates of the dynamic stiffness, k, can be determined by using Eqs. (19) and/or (20) with the resonance or anti-resonance frequencies identified from the magnitude and/or phase of the direct and/or transfer accelerance.

The measured direct and transfer accelerance are shown on Figure 7. The anti-resonance occurs in the direct accelerance at 79Hz. The first peak in the direct and transfer accelerance corresponds to the mass-spring-mass resonance frequency and occurs at 162Hz. The model described by equivalent circuit theory for the direct accelerance (Eq.(16)) is fitted to the measured data by measuring the half-power bandwidth to obtain the damping loss factor at resonance and minimising the differences between the measured and predicted resonance and anti-resonance frequencies in order to estimate the spring constant, k. This resulted in the stiffness of the four hangers in parallel as k=2.52MN/m, and a value of R corresponding to a loss factor, η=0.077. These values are then inserted into Eqs. (16) and (17) and plotted on Figure 7. The discrepancy between the two curves indicates that the resilient hanger does not behave exactly as a simple, linear spring, but that it is a reasonable approximation.

Brunskog and Hammer used their experimental set-up to improve estimates of the spring stiffness at high frequencies when it acts as a one-dimensional wave continuum. For the resilient hanger in this work, additional measurements are therefore carried out with different upper masses and the model is fitted to the data for the largest upper mass. These additional measurements indicate that above the mass-spring-mass resonance frequency the high frequency peaks shift as the magnitude of the upper mass is altered. However, the high frequency model from Brunskog and Hammer predicts resonance peaks which do not vary when using different upper masses. Hence it is not possible to find realistic values for the Helmholtz number corresponding to rubber that would give good agreement between

11

measurements and the high frequency model. It is therefore considered unlikely that a model for a one-dimensional wave continuum would be applicable to this resilient hanger, particularly because the metal fixing braces are only separated by 6.5mm thick rubber. An additional complication is that above 1kHz there is rocking motion in the test set-up which prevents use of the accelerance data to determine a frequency-dependent stiffness. For this reason only the mass-spring-mass resonance frequency is used to estimate the dynamic stiffness of the resilient hanger and this is applied across the entire frequency range used in the SEA models.

5. Experimental determination of loss factors

Due to the complexity of the timber-concrete composite floor it is necessary to incorporate some measured loss factors in the SEA models as described in this section.

5.1 Total loss factor for the rooms

The reverberation times for the rooms are measured according to ISO 10140-2 [13] from which the TLFs are calculated using [8]

$$\eta_i = \frac{2.2}{fT_i} \tag{21}$$

where T_i is the reverberation time of subsystem i.

5.2 Total loss factor for the floor cavity

Previous reverberation time measurements on cavities inside timber joist floors [8] and wall cavities [25] have shown that it is difficult to accurately predict the cavity TLF and that it is usually necessary to use measured reverberation times to calculate the TLF. One of the cavities in the floor is used for the reverberation time measurements. A loudspeaker (Fostex 6301B) is placed inside the cavity and the measured decay times averaged from two source positions and eight receiver positions for each source position, with signal processing carried out using M-Reverb with an MLS signal.

5.3 Coupling loss factor between a timber joist and the plasterboard ceiling across the resilient hangers

An alternative method to determine the CLF between the timber joist (subsystem i) and plasterboard ceiling (subsystem j) across the resilient hangers is considered with a two-subsystem SEA model [8]

$$\eta_{ij} = \frac{m_j \langle v_j^2 \rangle}{m_i \langle v_i^2 \rangle} \eta_j \tag{22}$$

where m is the mass and $\langle v^2 \rangle$ is the spatial average mean-square velocity for bending wave motion.

A small mock-up of the ceiling is built in the laboratory as shown in Figure 8. It comprises two 4000mm long, 260mm deep, 80mm wide timber joists that are attached to four timber noggins on a

2000mm x 980mm sheet of 12.5mm plasterboard using four suspended ceiling hangers on each joist. The joist width and depth are the same as those of the actual floor. The dimensions of the plasterboard are chosen to represent the static load that is supported by each hangar in the actual floor. The material properties are given in Table 1. As there are four resilient hangers per joist, Eq. (22) is scaled up to represent the total number of hangers in the floor, by dividing by four and multiplying by the number of resilient hangers for the whole floor (i.e. 56).

The timber joist is excited with an electrodynamic shaker (Gearing and Watson Electronics Type 6WV46) and the vibration level difference is measured between the timber joist and the plasterboard using accelerometers (PCB Type M352C65). All signal analysis is carried out using a Norsonic 840 analyser. The structural reverberation times of the plasterboard sheet are measured using the Norsonic 840 analyser with an MLS signal and time reversal to determine the total loss factor of the plasterboard.

6. Subsystem properties for the combination of concrete, OSB and timber joists

To form the concrete-OSB plate, the concrete is cast directly onto the OSB. However, it is not known whether the concrete and OSB would undergo bending vibration as a homogeneous unit over the frequency range from 50Hz to 5kHz. For this reason the vibration level difference is measured between the concrete and the OSB as described in section 6.1 to assess whether the concrete-OSB plate can be considered as a single SEA subsystem.

For SEA model 1, a single subsystem is used to represent the combination of concrete and OSB using the equivalent properties described in section 6.2. For SEA model 2a, a single subsystem is used to represent the combination of concrete, OSB and timber joists as described in section 6.3 using the approach of Kimura and Inoue. For SEA model 2b and 2c, a single subsystem represents the combination of concrete, OSB and timber joists as described in section 6.4 using the approach of Huffington and Troitsky. All material properties are given in Table 1.

6.1 Velocity level difference between the concrete and OSB

The velocity level difference between the concrete and OSB is measured using (1) mechanical excitation with an electrodynamic shaker (B&K Type 4809) attached using a threaded stud at three positions on the concrete and three positions on the OSB (these positions are at least 1m apart) and (2) airborne excitation with two loudspeaker positions in the room facing the concrete surface and also in the room facing the OSB surface (before the suspended ceiling was installed). Acceleration levels are measured using accelerometers (B&K Type 4513-B-002) at twelve random positions on both the source and receiving subsystems using a multi-channel analyser (Müller BBM PAK). These

accelerometers weigh 8.7g but the effect of mass loading from the accelerometer on the OSB is estimated to change the measured vibration levels by less than 1dB up to 5kHz [8].

Velocity level differences between the excited side and the other side of the concrete-OSB plate are shown in Figure 9. Between 50Hz and 630Hz the velocity level difference between the OSB and the concrete is <6dB. Above 630Hz the differences rapidly increase which indicates that the OSB and concrete do not behave as a single subsystem supporting bending wave vibration.

The above findings indicate that SEA model 1 will be appropriate up to 630Hz, but errors might occur at higher frequencies due to the assumption that the concrete-OSB acts as a single plate. However, there are two reasons why the vibration could be primarily transmitted from the concrete to the joists, rather than from the OSB to the joists. Firstly, the concrete, OSB and timber joists are all connected together by shear connectors. Secondly, for the connection between the concrete and OSB, approximately one-third of the top of each joist is in contact with the concrete and two-thirds is in contact with the OSB. For these reasons, any errors in the predicted sound insulation due to the velocity level difference between the concrete and OSB are expected to be negligible and this is confirmed by the results presented in Section 7.

6.2 SEA model 1: Concrete-OSB plate with equivalent thickness, density and Young's modulus

The combination of concrete and OSB can be modelled to give an equivalent density, ρ_{eq}, equivalent Young's modulus, E_{eq}, and equivalent thickness, h_{eq}, following the approach of Kimura and Inoue [14]. Considering the second moment of area for the concrete and OSB (I_1 and I_2 respectively) and combined cross-sections (I_{total}) gives these values as:

$$\rho_{eq} = \frac{\rho_1 h_1}{h_1 + h_2} + \frac{\rho_2 h_2}{h_1 + h_2} \tag{23}$$

$$E_{eq} = (E_1 I_1 + E_2 I_2)/I_{total} \tag{24}$$

$$h_{eq} = h_1 + h_2 \left(\frac{\rho_2}{\rho_1}\right) \tag{25}$$

$$I_{total} = \iint_A z^2 \mathrm{d}x\mathrm{d}z \tag{26}$$

where ρ is the density, h is the thickness, E is the Young's modulus, subscript 1 indicates the concrete and subscript 2 indicates the OSB.

These equivalent values are used to calculate the driving-point mobility of the plate, Y_{dp}, using Eq. (14) in section 4.3 in order to determine mechanical coupling across the point connections.

6.3 SEA model 2a: Combination of concrete, OSB and timber joists with equivalent thickness, density and Young's modulus

Following the approach of Kimura and Inoue [14] it is possible to model the combination of concrete, OSB and timber joists to give an equivalent density, equivalent Young's modulus and equivalent thickness. The limitations of this approach are that it only considers the stiffness in the direction parallel to the beams (i.e. joists); hence caution must be exercised when using equivalent values to calculate parameters other than the point impedance because the calculated equivalent parameters may differ significantly from the actual values.

For the cross-section of the floor shown on Figure 10a, the equivalent density, equivalent Young's modulus and equivalent thickness for the combination of concrete, OSB and timber joists are given by

$$\rho_{eq} = \frac{\rho_1 S_1}{S_1 + S_2 + S_3} + \frac{\rho_2 S_2}{S_1 + S_2 + S_3} + \frac{\rho_3 S_3}{S_1 + S_3 + S_3} \tag{27}$$

$$E_{eq} = (E_1 I_1 + E_2 I_2 + E_3 I_3)/I_{total} \tag{28}$$

$$h_{eq} = \sqrt[3]{12 I_{total}} \tag{29}$$

where S is the cross-sectional area of the materials, I_{total} is the second moment of area, subscript 1 indicates the concrete, subscript 2 indicates the OSB and subscript 3 indicates the timber joists. As in section 6.2, these values can be used to determine the driving point mobility using Eq. (14). A drawback of this approach is that if the equivalent values are very different to the concrete plate values, then they may not be appropriate to calculate the coupling loss factors for sound radiation from the plate to the room.

6.4 SEA model 2b and 2c: Equivalent isotropic plate and orthotropic plate

For the timber-concrete composite floor, the bending wavelength, λ_B, on the concrete-OSB plate is equal to the beam (i.e. joist) spacing, d_R, in the 3.15kHz one-third octave band. Hence $d_R < \lambda_B$ over the majority of the building acoustics frequency range (50Hz to 5kHz) therefore it is reasonable to consider a model for an equivalent orthotropic plate based on the bending stiffness in the directions parallel and perpendicular to the beams.

When the beam spacing is smaller than the bending wavelength ($d_R < \lambda_B$), an approach from Huffington [15] can be used to calculate an upper bound for the bending stiffness, B_x, in the x-direction perpendicular to the beams. For each repeating cross-section of length, d_R, the strain energy of the

equivalent plate is assumed equal to the strain energy of the actual plate. The strain energy of the equivalent plate, U_x, is

$$U_x = \int_{-d_R/2}^{d_R/2} \frac{d_R M_I^2}{2B_x} \, dx \qquad (30)$$

and the strain energy of the actual plate, U_a, is

$$U_a = \int_{-d_R/2}^{d_R/2} \frac{d_R M_I^2}{2E_a(x)I_a(x)} \, dx \qquad (31)$$

where the bending moment, M_I, is the same for each repeating section and $E_a(x)$ and $I_a(x)$ are the Young's modulus and second moment of area as functions of x respectively.

For the timber-concrete composite floor the cross-section is a simple T-section; hence the integral can be separated into parts where $E_a(x)$ and $I_a(x)$ are constant to estimate the upper bound for B_x. Setting Eqs. (30) and (31) to be equal gives B_x by considering the concrete (subscript 1) forming the plate and the timber joists (subscript 2) where

$$\frac{B_x}{d_R} = \int_{-d_R/2}^{-d_y/2} \frac{1}{E_1 I_A} \, dx + \int_{-d_y/2}^{d_y/2} \frac{1}{E_1 I_C - E_2 I_D + E_2 I_E} \, dx + \int_{d_y/2}^{d_R/2} \frac{1}{E_1 I_B} \, dx \qquad (32)$$

where $I_A = I_B = I_C = I_D = \frac{h^3}{12}$ and $I_E = \frac{d_z^3}{12}$, h is the thickness of the concrete and OSB plate (see Figure 10b) and d_z is the full depth of the floor as indicated in Figure 10b.

For the timber-concrete composite floor it is possible to consider only the concrete and the timber joists because the OSB has negligible influence on the resulting bending stiffness. Hence B_x can be calculated from

$$B_x = \frac{d_R h^3}{12} \left[\frac{E_1 \left(E_1 h^3 + E_2 (d_z^3 - h^3) \right)}{(d_R - d_y) E_2 (d_z^3 - h^3) + d_R E_1 h^3} \right] \qquad (33)$$

where subscript 1 indicates the concrete and subscript 2 the joists. The geometry for the calculations is shown in Figure 10b. If the floor geometry is more complex, then an 'effective thickness' approach from Huffington [15] can be used to calculate the bending stiffness in the x-direction perpendicular to the beams. Setting Eqs. (30) and (31) to be equal, keeping $E_a(x)$ constant (in this case setting it to E_1, the Young's modulus of the concrete) and varying $I_a(x)$ results in a general equation for B_x, given by

$$B_x = \frac{E_1 I_1}{\frac{h^3}{d_R} \int_{-d_R/2}^{d_R/2} \frac{dx}{h_a^3(x)}} \qquad (34)$$

where $h_a(x)$ is a continuously-variable effective plate thickness which is equivalent to the actual ribbed plate. An advantage with this approach is that it can be used for unusual cross-sections and in situations where the plate and beams consist of different materials.

The bending stiffness in the y-direction parallel to the beams is calculated from Troitsky [16] using

$$B_y = \frac{E_1 h^3}{12(1 - v^2)} + \frac{E_1 h z_y^2}{(1 - v^2)} + \frac{E_2 I_2}{d_R} \tag{35}$$

where z_y is the distance from the mid-plane of the plate to the neutral axis which is calculated according to

$$z_y = \frac{\iint_A E(z) z \, dy \, dz}{\iint_A E(z) \, dy \, dz} \tag{36}$$

where $E(z)$ is the elastic modulus as a function of z, in this case a function which can be expressed with respect to the central plane of the plate as

$$E(z) = E_1 \text{ where } -\frac{h}{2} < z < \frac{h}{2}$$

$$E(z) = E_2 \text{ where } \frac{h}{2} \le z \le \left(d_z - \frac{h}{2} \right) \tag{37}$$

For the concrete plate (subscript 1) with timber joists (subscript 2), B_y is given by

$$B_y = \frac{E_1 h}{(1 - v^2)} \left[\frac{h^3}{12} + z_y^2 \right] + d_y \frac{E_2}{d_R} (d_z - h) \left[\frac{(d_z - h)^2}{12} + \left(\frac{d_z}{2} - z_y \right)^2 \right] \tag{38}$$

where

$$z_y = \frac{E_2 (d_z^2 - d_z h) d_y}{2 \left(E_1 h d_R / (1 - v^2) + E_2 (d_z - h) d_y \right)} \tag{39}$$

An effective bending stiffness can be calculated from B_x and B_y which allows the orthotropic plate to be modelled as an equivalent isotropic plate using

$$B_{\text{eff}} = \sqrt{B_x B_y} \tag{40}$$

Eq. (37) can be used to estimate the driving-point mobility of the plate by replacing B with B_{eff} in Eq. (14).

6.5 Comparison of calculated subsystem properties

Table 2 gives the properties for (1) the concrete plate, (2) the combination of concrete and OSB and (3) the combination of concrete and timber joists.

The difference between the bending stiffness for the combined concrete-OSB plate and the concrete by itself is 18%. However, the percentage difference is significantly larger for the combination of concrete, OSB and timber joist T-section (Kimura and Inoue), the orthotropic plate parallel to the beams (Troitsky) and the equivalent isotropic plate (Huffington and Troitsky). The bending stiffness calculated using Troitsky may also be regarded as an upper limit because it takes into account the full depth of the beams.

The orthotropic plate calculations according to Huffington and Troitsky result in bending stiffnesses for directions parallel and perpendicular to the beams that differ by more than a factor of ten; this gives rise to two critical frequencies of 63Hz and 232Hz. The bending stiffness parallel to the beams differs from the concrete by 1665% when calculated according to Troitsky, and 1097% for the combination of concrete, OSB and timber joist T-section when calculated according to Kimura and Inoue. The equivalent and effective bending stiffnesses can be used to calculate the mobility of the combination of concrete, OSB and timber joists using Eq. (14) and thus the coupling loss factor across the resilient hangers to the plasterboard according to Eq. (13). For SEA models 2a and 2b these coupling loss factors are shown on Figure 11. Using the Kimura and Inoue model results in a coupling loss factor that is ≈2.3dB lower than the Huffington and Troitsky model.

The fundamental mode of the concrete-OSB plate is estimated as being below 50Hz using both the Huffington and Troitsky and Kimura and Inoue models. For this reason the SEA model can be used to predict the performance over the building acoustics frequency range from 50Hz to 5kHz.

7. Results

7.1 Total loss factor for the cavity

The measured cavity reverberation times are shown in Figure 12 for one cavity inside the floor that was installed in the sound transmission laboratory. The first cross-cavity mode occurs in the 630Hz one-third octave band, and above this frequency band the average reverberation time is shorter than the average reverberation time of the frequency bands below 630Hz.

7.2 Coupling loss factor between a timber joist and the plasterboard ceiling across the resilient hangers

In SEA model 1, the timber joists are modelled as a single subsystem; hence it is beneficial to validate the predicted coupling across the resilient hangers from the timber joists to the plasterboard. This coupling loss factor is calculated from the measured dynamic stiffness of the resilient hanger as described in sections 4.3 and 4.32, and measured as described in section 5.3. Figure 13 shows that below 160Hz the measured coupling loss factor is significantly lower than predicted (which might be attributed to strong coupling from the first two beam modes) but that there is reasonable agreement between 160Hz and 1kHz. Above 1kHz the measured coupling loss factor tends to plateau and this feature is not evident in the predicted coupling loss factor. This is likely to be due to the difficulty in accurately measuring the structural reverberation time in the region of the critical frequency of the plasterboard [8]. Due to the agreement in the mid-frequency range it is therefore considered appropriate to use the coupling loss factor calculated from the measured dynamic stiffness of the resilient hanger across the entire frequency range for all SEA models.

7.3 Comparison of SEA models with measurements

SEA models 1, 2a, 2b and 2c are compared against measured data in Figure 14. Note that the matrix inversion for SEA did not yield values for the 50Hz and 63Hz one-third octave bands.

All four SEA models show the same general trend with frequency as the measurements. For SEA models 1 (100Hz to 500Hz), 2a (100Hz to 500Hz), 2b (100Hz to 500Hz) and 2c (100Hz to 250Hz), the average differences in terms of magnitudes between measurements and predictions from the one-third octave band data are 3.0dB, 2.3dB, 2.8dB and 3.1dB respectively, and the average differences considering positive and negative values are 2.1dB, 1.5dB, 0.4dB and -3.1dB. These differences in terms of magnitude indicate that the average error is similar to that using SEA to predict airborne sound insulation with heavyweight building elements [8]. The differences in terms of positive and negative values are sufficiently close to 0dB that it is reasonable to expect that when the single-number quantities are calculated there will be close agreement between measurements and SEA.

The differences between models 1, 2a, 2b, and 2c at frequencies below 250Hz are due to the different critical frequencies (and hence radiation efficiencies) of subsystem 2. The models therefore have different plate to room resonant coupling loss factors, and subsystem 2 also has a lower modal density in models 2b and 2c. At and above 250Hz the differences between the models are due to the lower modal density of subsystem 2 in model 2b.

For lightweight cavity walls, Hongisto [26] compared seventeen different prediction models described in the literature. The average prediction errors for individual frequencies were as high as 20dB for most of the models, and less than 10dB for the best models. One of the main criticisms of these models was that they had limited application to actual building elements. Hence not only are the predictions for the timber-concrete composite floor with SEA significantly more accurate, but they also demonstrate that real floors (which are relatively complex constructions) can be modelled using SEA by incorporating some measured loss factors in the model.

The single-number quantities in terms of $R_w(C;C_{tr})$ are rated using ISO 717-1 [27] over the frequency range from 100Hz to 3.15kHz. $R_w(C;C_{tr})$ is 58(-2;-9) dB for the laboratory measurement, and 56(-1;-6) dB, 57(-2;-7) dB and 58(-3;-10) dB for SEA models 1, 2a and 2b respectively; hence the maximum error of the SEA models in predicting R_w is 2dB. The adverse deviations that occur in the calculation of the single-number quantity are between 100Hz and 400Hz for the measurement, between 100Hz and 630Hz for SEA models 1 and 2a, and between 100Hz and 500Hz for model 2b. Hence for single-number quantities it is more important for the SEA model to provide accurate predictions at and below 630Hz rather than in the high-frequency range.

The trends predicted by SEA models 1, 2a and 2b are in agreement with measurements over the entire frequency range from 100Hz to 3.15kHz, and SEA model 2c is in agreement between 80Hz and 250Hz. Model 2b predicts the closest single figure values due to close agreement over the low frequency range (100-500Hz). For SEA model 2c the Huffington and Troitsky model for the combination of concrete, OSB, and timber joists indicates that the plate is highly orthotropic with two critical frequencies of 63Hz and 232Hz; in fact the measurements do indicate slight dips in the sound reduction index in the 63Hz and 200Hz bands which are near these two critical frequencies. In practice, SEA model 2c provides a reasonable estimate of the upper bound to the sound reduction index when compared with the measured data because it uses an upper bound to determine the bending stiffness.

When considering the application of the orthotropic plate models to other similar framed or ribbed plate constructions there are some limitations to be considered. SEA model 2a does not take account of the bending stiffness perpendicular to the joists and a potential disadvantage of using effective thickness, density and Young's modulus is that unusual shapes and deep beams could result in effective values that cannot be used to determine an appropriate radiation efficiency. For this reason, model 2b is preferred because the approach of Huffington and Troitsky is well-suited to multi-layer plates with complex geometric cross-sections. To apply model 2c to other floors, the applicable frequency range might need to be extended. This could be achieved above and below the two critical frequencies by applying a more generally applicable model such as proposed by Leppington *et al* [28]. Additional theory could be developed to improve the prediction of non-resonant transmission between the critical frequencies as in this paper only Eq. (11) has been used.

For simple SEA models with only a few dominant transmission paths where the combination of all the other paths is negligible, the sum of the dominant transmission paths is approximately equal to the matrix solution to within 0.1dB [22]. This situation does not occur with SEA model 1 as a result of the strong coupling between the concrete and the timber beam subsystems. However, this does occur for SEA models 2a, 2b and 2c. Hence for SEA model 2b, Figure 15a allows comparison of the relative strengths of different transmission paths from SEA path analysis. The crossover between the 1D and 3D non-resonant models for sound transmission into and out of the cavity occurs at 500Hz and therefore two predicted data points occur in this one-third octave band. Figure 15b shows the corresponding matrix SEA results for model 2b.

From 50Hz to 100Hz the dominant transmission path is 1→3→5. Unfortunately the matrix solution is invalid for the 50Hz and 63Hz one-third octave bands; hence no values are shown in these bands although path 1→3→5 gives an indication of the overall sound reduction index. From 125Hz to

400Hz the strongest paths are 1→2→3(1D)→5 and 1→2→4→5. From 500Hz to 1.6kHz the main paths are 1→2→3(2D/3D)→5 and 1→2→4→5. At and above 2kHz the strongest paths are 1→2→3(2D/3D)→4→5 and 1→2 →4→5.

Based on SEA model 2b, identification of the dominant paths indicates how the airborne sound insulation could be increased. Below 100Hz this would require increasing the mass of the concrete-OSB and/or the plasterboard to reduce non-resonant transmission from the rooms to the cavities along path 1→3→5. Above 100Hz, an extra layer of plasterboard on the ceiling and completely filling the cavity with porous material would reduce the strength of paths 1→2→3→5, 1→2→4→5 and 1→2→3→4→5.

The predicted dip in the sound reduction index near the 2kHz one-third octave band due to the critical frequency of the plasterboard is not evident in the measured data although there is a shallow dip in the 2.5kHz band. However, it is common for measured and predicted sound insulation to differ near the critical frequency, partly due to uncertainty in the range of angles of incidence that exist near grazing and partly because of the empirical approach used to limit all the radiation efficiency values to a value of one [8].

8. Conclusions

SEA models have been developed to predict airborne sound insulation across a timber-concrete composite floor with a suspended ceiling. The large number of nails and shear connectors connecting the concrete, OSB and timber joists in this floor required consideration of two different types of SEA model. A six-subsystem model treated the concrete-OSB plate as a single subsystem with point connections to the joist and three different five-subsystem models treated the combination of concrete, OSB and timber joists as a single subsystem. All the models were experimentally validated against laboratory measurements and were able to predict the weighted sound reduction index to within 2dB. For the comparison of measurements and predictions in one-third octave bands, the average difference (magnitude) was up to 4.3dB. These results add to a growing body of evidence [8,9,25] indicating that SEA can be used to model direct transmission across realistic cavity wall/floor constructions found in buildings with greater accuracy than many analytical models. However, this requires the inclusion of some measured parameters in the SEA model. For the timber-concrete composite floor, measured data was needed for the dynamic stiffness of the resilient isolators and the reverberation time in the cavity. Compared to some analytical or deterministic models, path analysis with SEA provides straightforward insights into the dominant transmission mechanisms and this simplifies the process of identifying design changes to improve the sound insulation.

To model similar ribbed plates with SEA when it is ambiguous whether the upper plate and the ribs should be modelled as separate subsystems or as a single orthotropic plate subsystem, it is recommended that both models are created and compared with measurements. For the orthotropic plate model it is suggested that bending stiffnesses predicted using the theories of Huffington and Troitsky provide a more suitable and flexible approach than that of Kimura and Inoue. This is primarily because (1) the latter does not take account of the bending stiffness perpendicular to the joists, (2) it is not suited to modelling the stiffening effect of the beams when predicting sound radiation and (3) the approach of Huffington and Troitsky is better suited to multi-layer plates with complex geometric cross-sections. Further work could investigate the application of these models to impact sound insulation.

Acknowledgements

References

[1] M. Van Damme, M. Blasco, C. Crispin, P. Huart, B. Ingalaere, D. Wuyts. Acoustic comfort in timber frame dwellings. Journal of Building Acoustics 2007;14(1):15-24.

[2] J. S. Bradley, J. A. Birta. On the sound insulation of wood stud exterior walls. Journal of the Acoustical Society of America 2001;110 (6):3086-3096.

[3] D. Wuyts, C. Crispin, B. Ingelaere, M. Van Damme. Laboratory sound insulation measurements of improved timber floor constructions: A parametric survey. Journal of Building Acoustics 2006;13(4):311-325.

[4] L. J Hu, Y. H Chui and D. M. Onysko. Vibration serviceability of timber floors in residential construction. Progress in Structural Engineering and Materials 2001;3:228-237.

[5] D. Yeoh, M. Fragiacomo, M. De Franceschi, K.H. Boon. State of the art on timber-concrete composite structures: Literature review. Journal of Structural Engineering 2011;137(10):1085-1095.

[6] J. Forssén, W. Kropp, J. Brunskog, S. Ljunggren, D. Bard, G. Sandberg, F. Ljunggren, A. Ågren, O. Hallström, H. Dybro, K. Larsson, K. Tillberg, K. Jarnerö, L-G. Sjökvist, B. Östman, K. Hagberg, Å. Bolmsvik, A. Olsson, C-G. Ekstrand, M. Johansson. Acoustics in wooden buildings - State of the art 2008 - Vinnova project 2007-01653. SP Technical Research Institute of Sweden. SP Report 2008:16. ISBN 978-91-85829-31-6.

[7] C. Guigou-Carter, M. Villot, R. Wetta. Prediction method adapted to wood frame lightweight constructions. Journal of Building Acoustics 2006;13(3):173-188.

[8] C. Hopkins. Sound insulation, Butterworth-Heinemann, 2007. ISBN 978-0-7506-6526-1.

[9] R. J. M. Craik, R. S. Smith, Sound transmission through double leaf lightweight partitions part I: airborne sound. Applied Acoustics 2000;61:223-245.

[10] B.H. Sharp, Prediction methods for the sound transmission of building elements. Noise Control Engineering 1978;11:53-63.

[11] R.J.M. Craik and L. Galbrun. Vibration transmission through a frame typical of timber-framed buildings. Journal of Sound and Vibration 2005;281:763-782.

[12] S. Schoenwald. Flanking sound transmission through lightweight framed double leaf walls – Prediction using statistical energy analysis. Eindhoven University of Technology. PhD thesis (2008).

[13] ISO 10140-2:2010 Acoustics - Laboratory measurement of sound insulation of building elements - Part 2: Measurement of airborne sound insulation. International Organisation for Standardisation.

[14] S. Kimura and K. Inoue. Practical calculation of floor impact sound by impedance method. Applied Acoustics 1989;26:263-292.

[15] N. J. Huffington. Bending athwart a parallel stiffened plate. Journal of Applied Mechanics 1967;34(2) :278-282.

[16] M. S. Troitsky. Stiffened plates: bending stability and vibrations. Elsevier, 1976. ISBN 0-444-41530-0.

[17] F.G. Leppington, E. G. Broadbent, K. H. Heron, S. M. Mead, Resonant and non-resonant acoustic properties of elastic panels I. The radiation problem. Proceedings of the Royal Society London 1986;A406:139-171.

[18] M. Heckl, Untersuchungen an Orthotropen Platten. Acustica 1960;10:109-115.

[19] R.J.M. Craik. Non-resonant sound transmission through double walls using statistical energy analysis. Applied Acoustics 2003;64:325-341.

[20] A.J. Price and M.J. Crocker. Sound transmission through double panels using statistical energy analysis. Journal of the Acoustical Society of America 1970;47(1/3):683-693.

[21] F.G. Leppington, K.H. Heron, E.G. Broadbent and S.M. Mead. Resonant and non-resonant acoustic properties of elastic panels. II. The transmission problem. Proceedings of the Royal Society, London 1987;A412:309-337.

[22] R.J.M. Craik. Sound transmission through buildings using statistical energy analysis. Gower, Aldershot (1996) ISBN 0566075725.

[23] J. Brunskog and P. Hammer. Measurement of the acoustic properties of resilient, statically tensile loaded devices in lightweight structures. Journal of Building Acoustics 2002;9(2):99-137.

[24] C. Hopkins, R. Wilson and R.J.M. Craik. Dynamic stiffness as an acoustic specification parameter for wall ties used in masonry cavity walls. Applied Acoustics 1999;58:51-68.

[25] C. Hopkins. Sound transmission across a separating and flanking cavity wall construction. Applied Acoustics 1997;52(3/4):259-272.

[26] V. Hongisto. Sound insulation of double panels – comparison of existing prediction models. Acta Acustica united with Acustica 2006;92:61-78.

[27] ISO 717-1:2013 Acoustics – Rating of sound insulation in buildings and of building elements – Part 1: Airborne sound insulation. International Organisation for Standardisation.

[28] F. G. Leppington, K. H. Heron, E. G. Broadbent, Resonant and non-resonant transmission of random noise through complex plates, Proceedings of the Royal Society London 2002;458:683-704.

Tables

Table 1. Material properties for the floor components that form plates and beams in the SEA model.

Floor component	Type of element	Thickness (mm)	Quasi-longitudinal wavespeed (m/s)	Density (kg/m^3)	Poisson's ratio (-)	Internal loss factor (-)
Concrete	Plate	70	3690[a]	2200[c]	0.2[c]	0.01[b]
OSB	Plate	12	2570[c]	590[c]	0.3[c]	0.01[c]
Plasterboard	Plate	12.5	2375[a]	1024[d]	0.3[c]	0.0125[c]
Timber joist	Beam	260	5775[a]	440[c]	0.3[c]	0.0156[b]

[a] Measured using time-of-flight (see section 3.11.3.5 in [8])

[b] Determined from measured structural reverberation times (see section 3.11.3.4 in [8]).

[c] From Table A2 in [8].

[d] Datasheet provided by manufacturer.

Table 2. Calculated bending stiffness, thickness, density, Young's modulus.

Method	Bending stiffness (Nm)	Equivalent thickness (m)	Equivalent density (kg/m^3)	Equivalent Young's modulus (N/m^2)	Difference in bending stiffness* (%)
Concrete plate	8.57x10^5	-	-	-	0
Concrete-OSB plate (Kimura & Inoue)	7.03x10^5	0.0732	1964	2.06x10^{10}	-18
Concrete-OSB-timber joist T-section (Kimura & Inoue)	1.03x10^7	0.1845	1407	1.88x10^{10}	1097
Orthotropic plate parallel to beams (Troitsky)	1.51x10^7	-	-	-	1665
Orthotropic plate perpendicular to beams (Huffington)	1.00x10^6	-	-	-	17
B_{eff} for an equivalent isotropic plate	3.89x10^6				354

*Relative to the value for the concrete plate
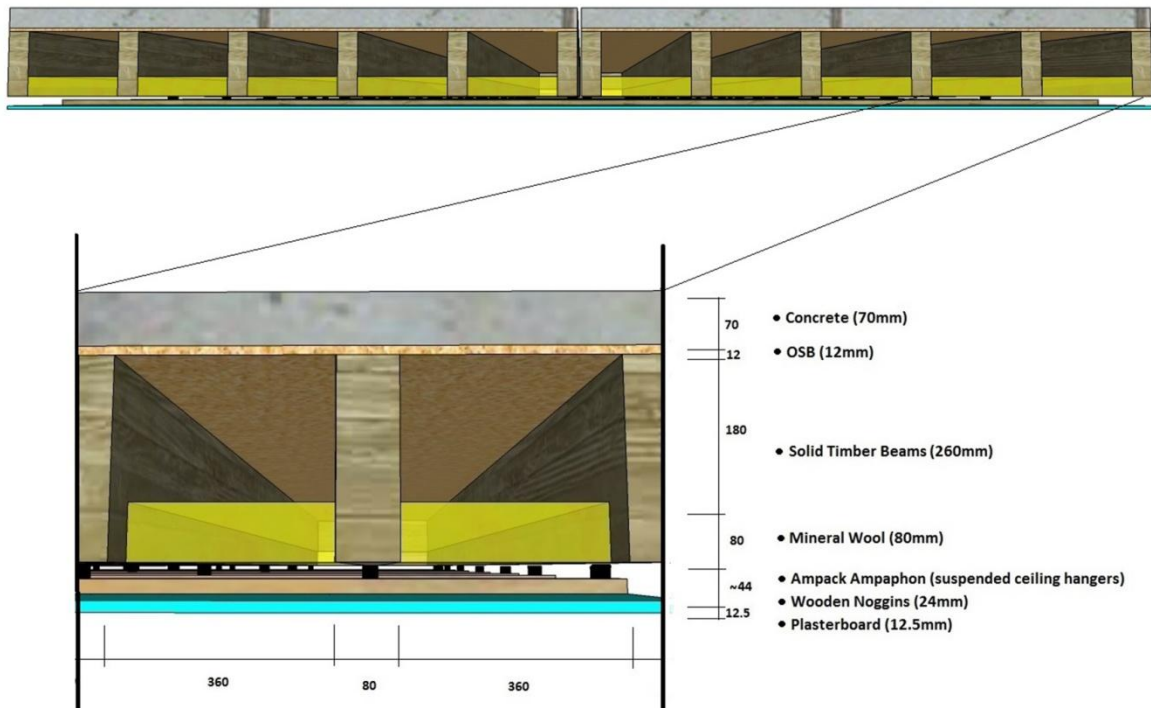
Figure 1. Cross section through the floor construction.
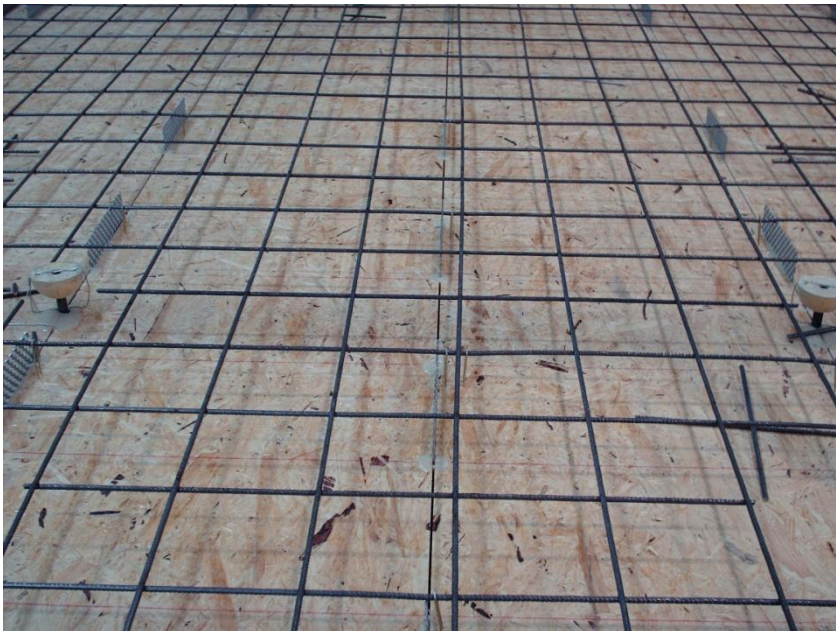
Figure 2. Lines of shear connecting strips protruding through the OSB before the concrete is cast on a nominally identical floor (NB This photo also shows the steel reinforcement mesh.).

Figure 3. Timber joist in contact with the concrete.
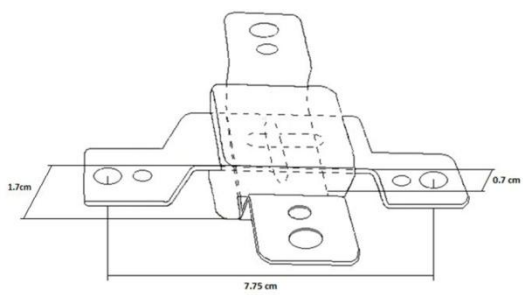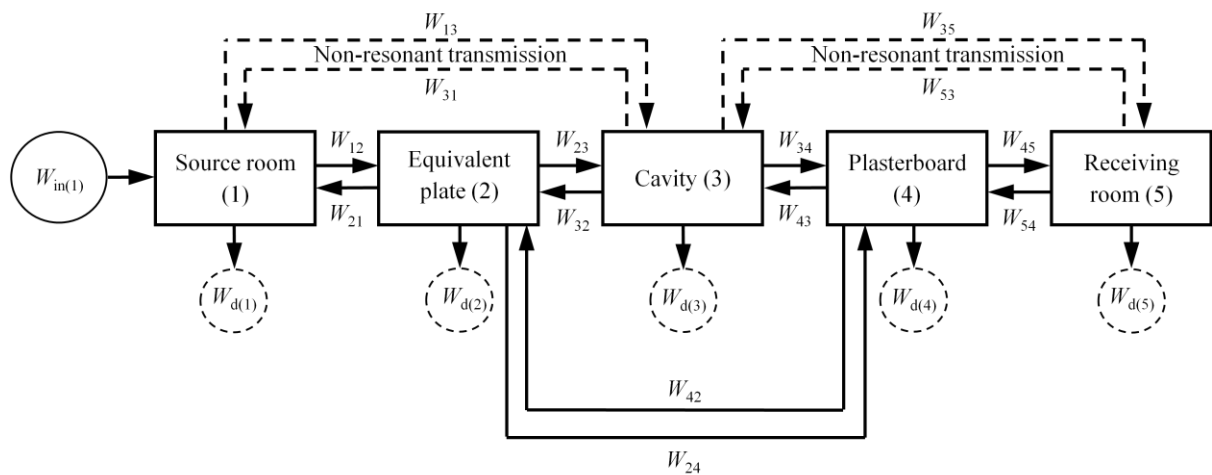

(a)

(b)
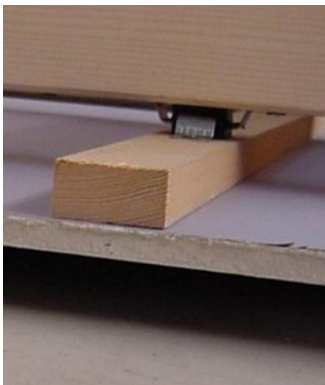
(c)

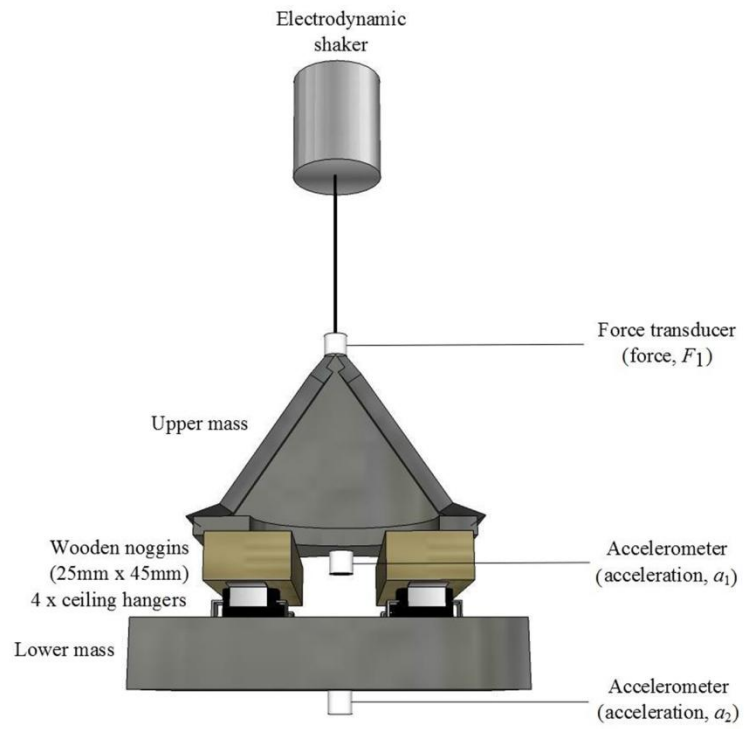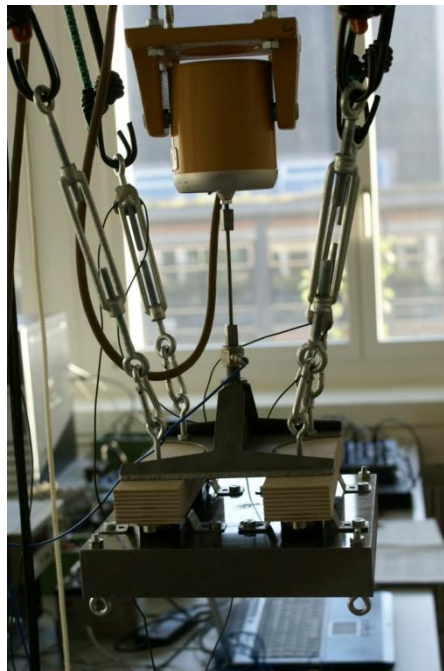**Figure 4.** Resilient hanger. (a) sketch with dimensions, (b) photo of actual hanger, (c) photo of hanger installed between a joist and a noggin.

(a)
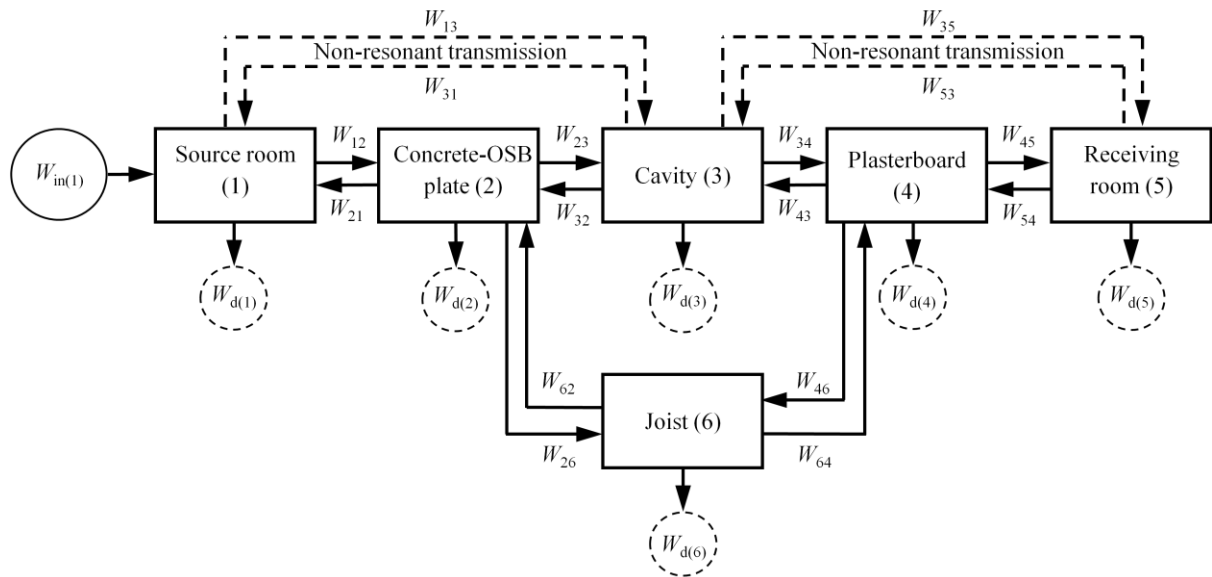
(b)

Figure 5. SEA modelling of the floor construction: (a) Model 1 (six subsystems), (b) Model 2 (five subsystems).

(a)

(b)

Figure 6. Test rig used to determine the spring stiffness: (a) sketch with labels, (b) photograph.

(a)
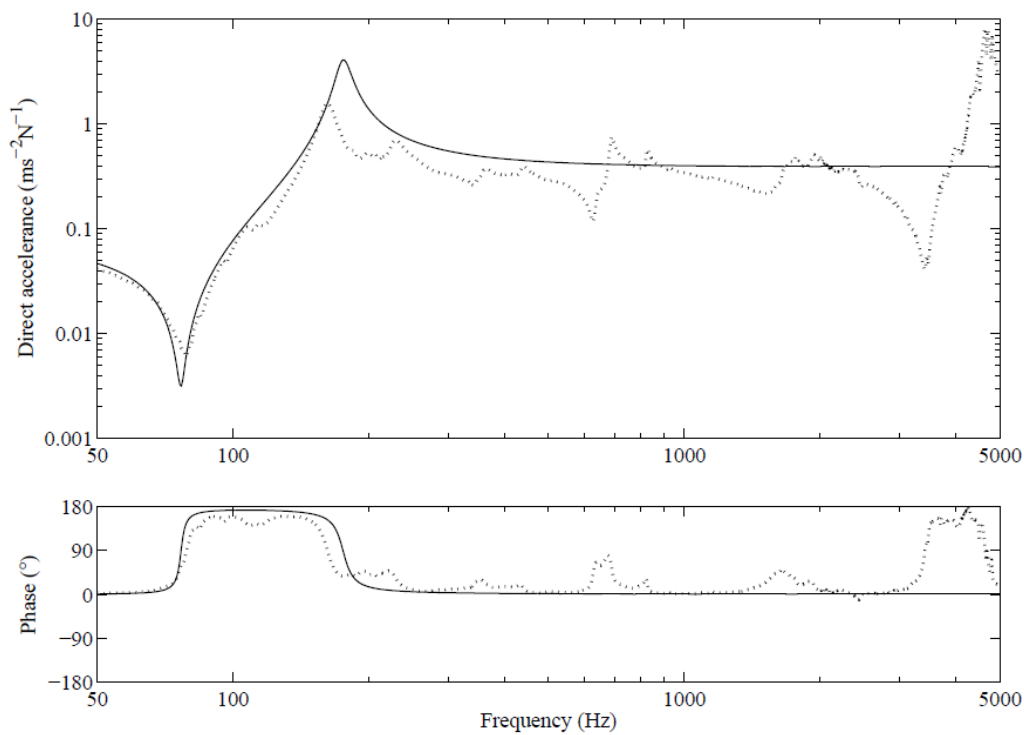
(b)
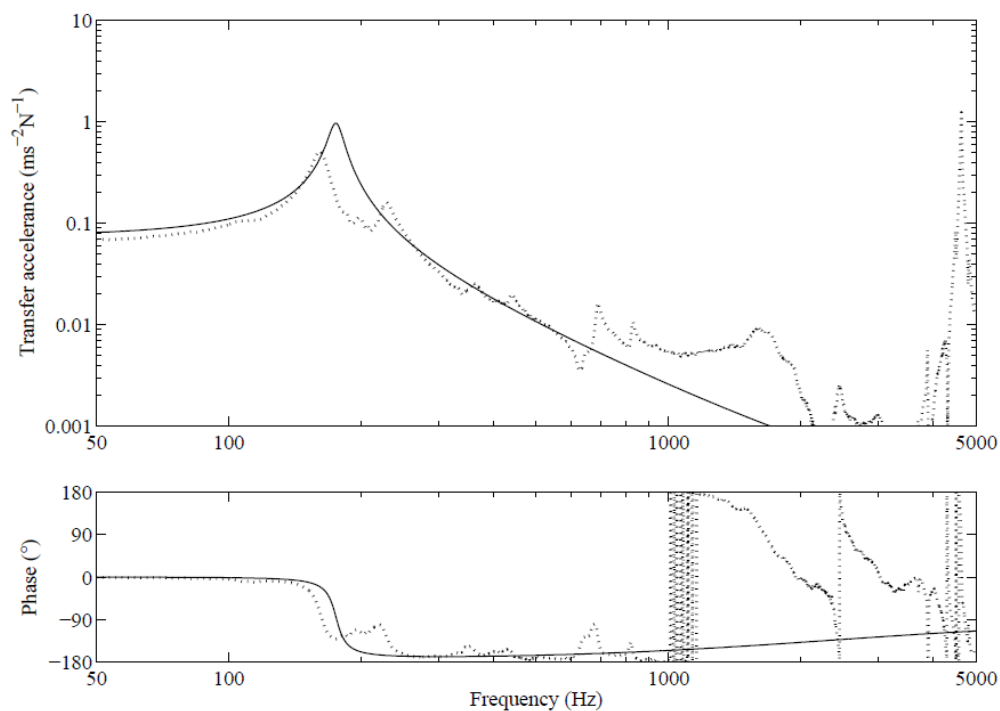
Figure 7. Measurements with the resilient hanger in the mass-spring-mass test set-up: (a) direct accelerance, (b) transfer accelerance. The dashed line indicates measured data. The solid line indicates calculated results from Eqs. (16) and (17) for (a) and (b) respectively using estimated values of dynamic stiffness and damping constant from the measured data.

Figure 8. Laboratory mock-up for measuring the CLF between the timber joists and the plasterboard ceiling across the resilient hangers.
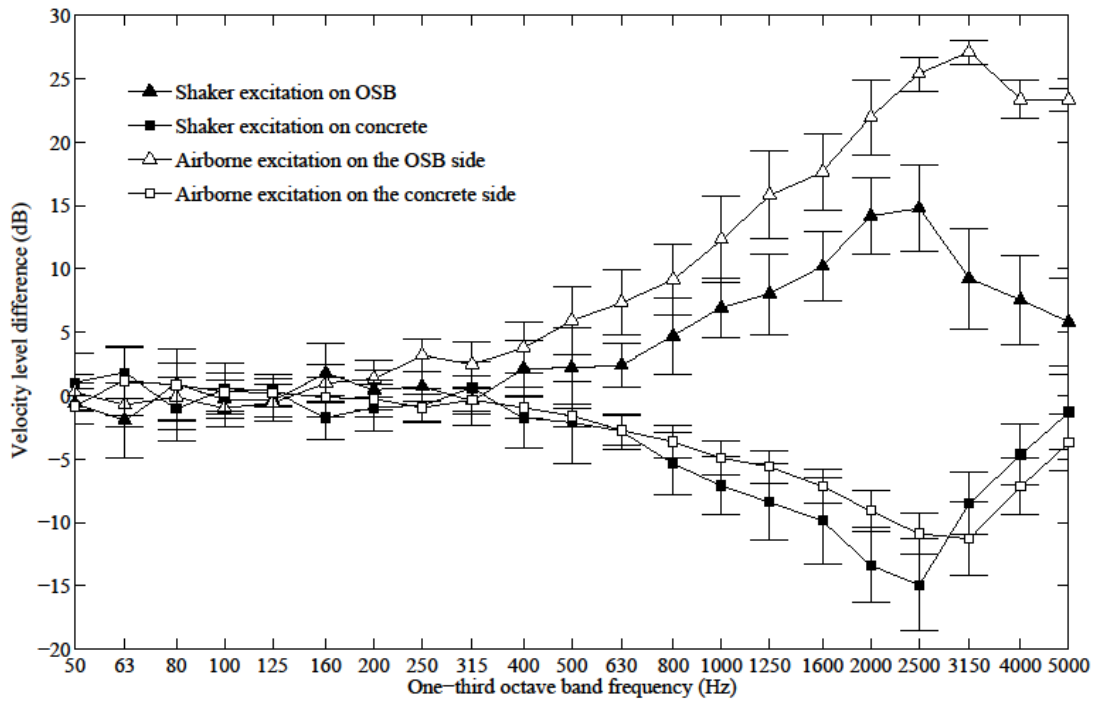
Figure 9. Velocity level difference between the concrete and the OSB with excitation on either the OSB or the concrete (95% confidence limits are indicated).
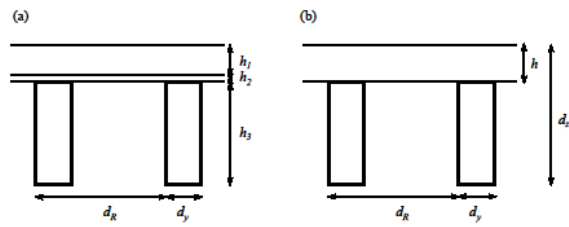
Figure 10. Cross-section of the concrete-OSB and timber joists showing dimensions for calculation of (a) equivalent thickness, density, Young's modulus, (b) equivalent bending stiffness.
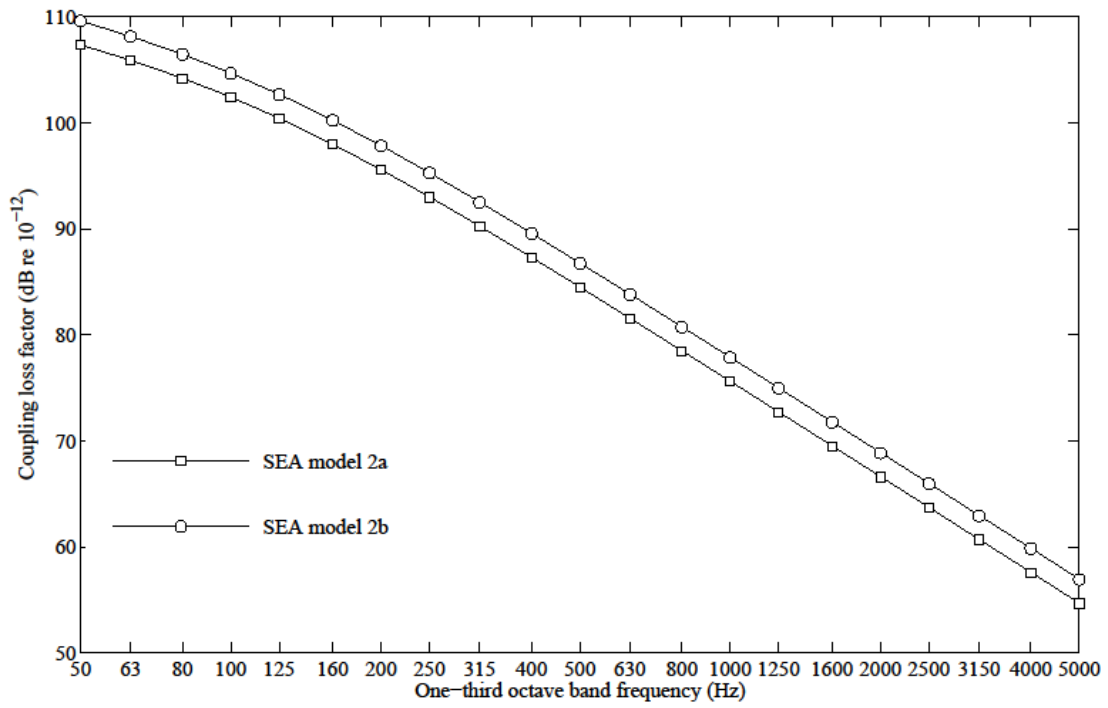
Figure 11. SEA model 2. Calculated coupling loss factors from the plate subsystem for models 2a and 2b representing the combination of concrete, OSB and timber joists to the plasterboard subsystem.
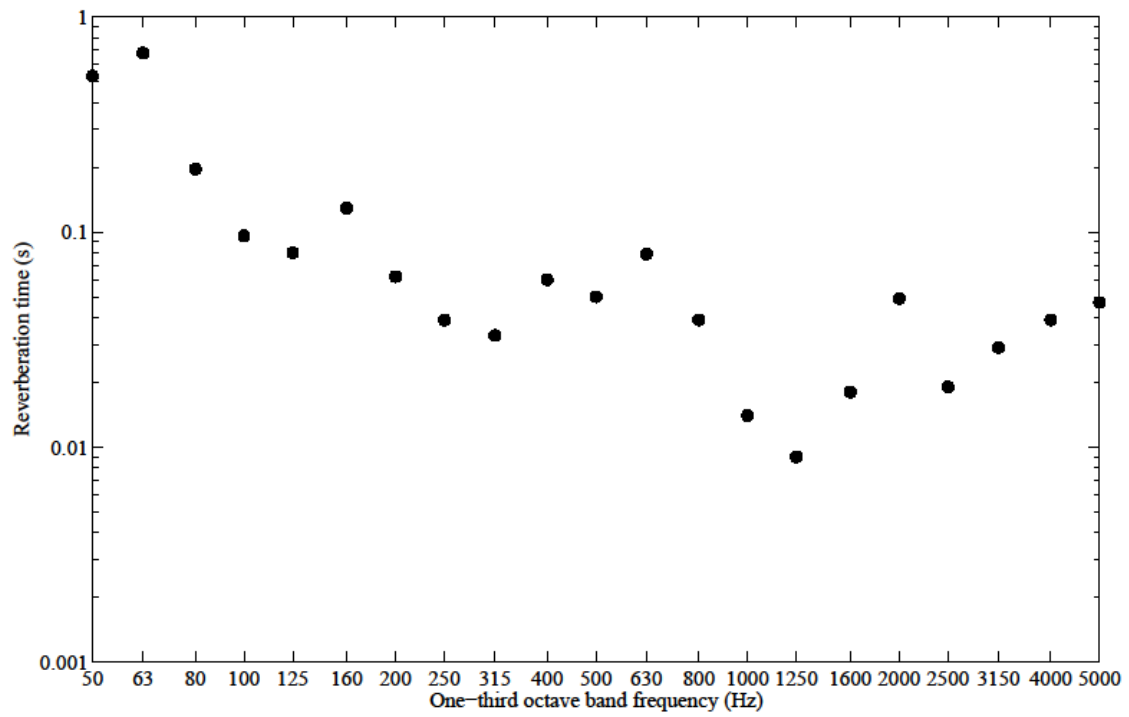
Figure 12. Measured reverberation times in one floor cavity.
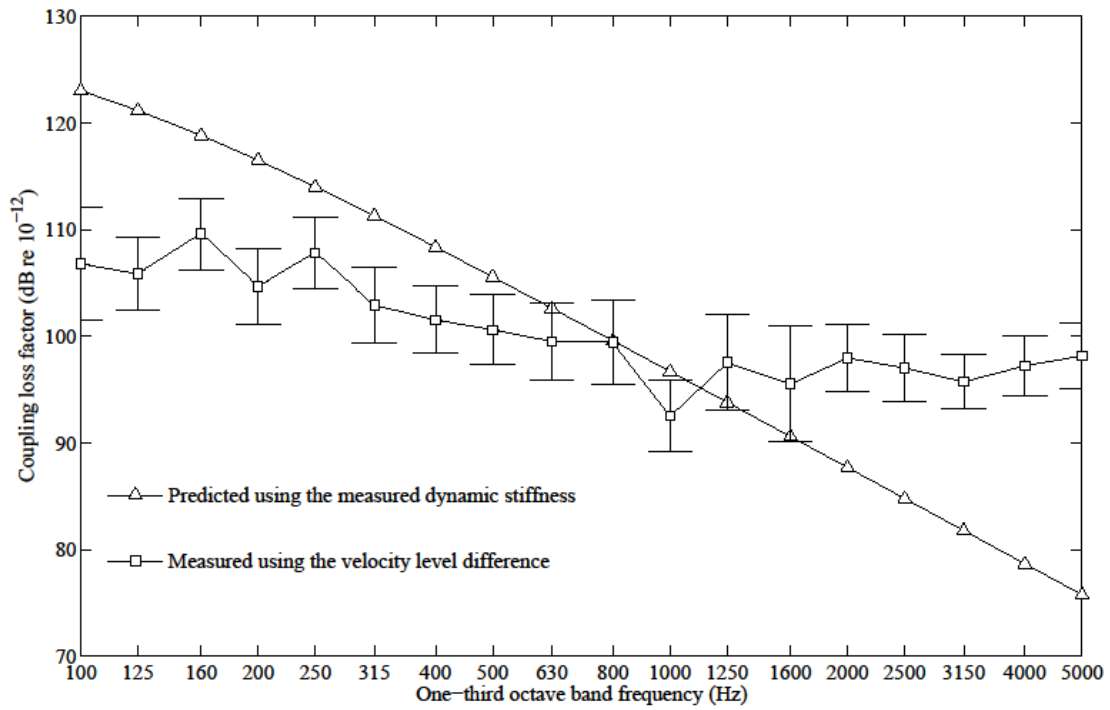
Figure 13. Coupling loss factors from a timber joist (beam) to the plasterboard ceiling (plate) predicted using the measured dynamic stiffness for the resilient hanger in Eq. (13) and measured using the velocity level difference as described in section 5.3 (95% confidence limits are indicated).
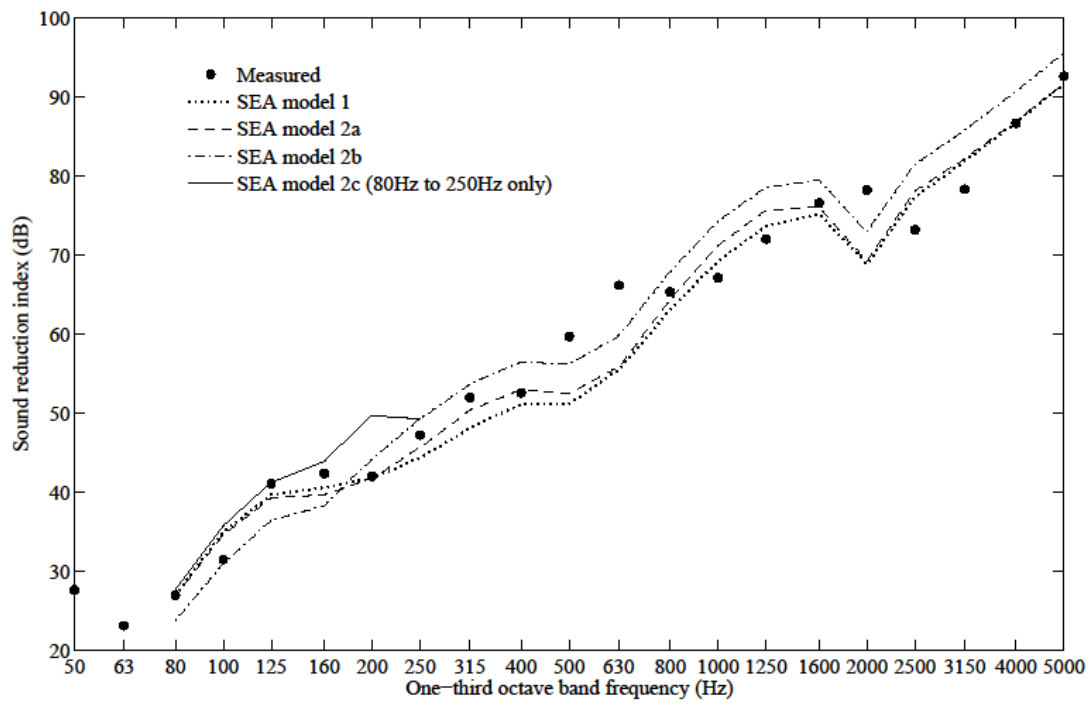
Figure 14. Comparison of the measured and predicted sound reduction index from the different SEA models.
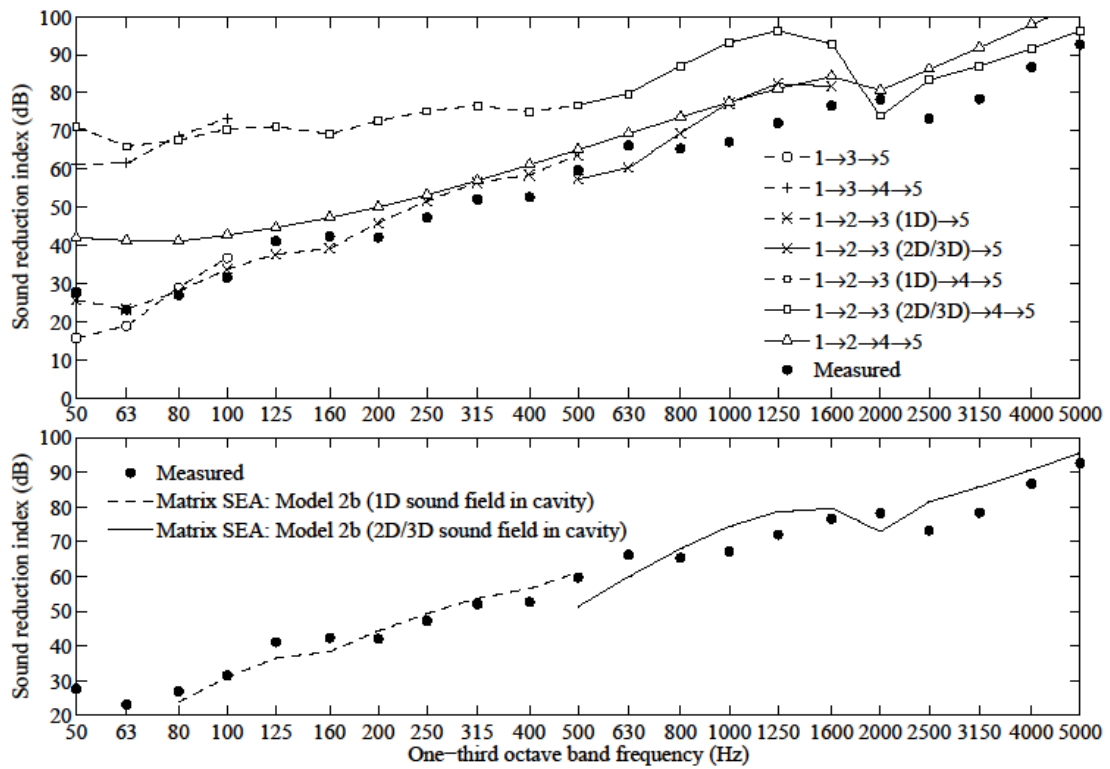
Figure 15. SEA model 2b: (a) comparison of SEA transmission paths with measurements, (b) comparison of matrix SEA with measurements.